Article

An Elaborated Study of CO Sensitivities of Cu, Pt and Pd Activated SnO_2 Sensors: Effect of Precipitation Agents, Dopants and Doping Methods

Venkata Krishna Karthik Tangirala [1,*], Heberto Gómez-Pozos [2], Ventura Rodríguez-Lugo [3], M. de la L. Olvera [1]

[1] Departamento de Ingeniería Eléctrica-SEES, Centro de Investigación y de Estudios Avanzados del Instituto Politécnico Nacional, CINVESTAV-IPN, Apartado postal 14740, México D. F. 07360, México. krishnakarthik.tv@gmail.com; molvera@cinvestav.mx.

[2] Área académica de Computación y Electrónica, ICBI, Universidad Autónoma del Estado de Hidalgo, Hidalgo, 56092, México. gpozos@uaeh.edu.mx.

[1] Área Académica de Ciencias de la Tierra y Materiales, Instituto de Ciencias Básicas e Ingeniería, Universidad Autónoma del Estado de Hidalgo, Carretera Pachuca-Tulancingo Km. 4.5, 42184. Hidalgo, México. ventura.rl65@gmail.com.

* Correspondence: krishnakarthik.tv@gmail.com ; Tel.: +52-553-194-7927

Abstract: In this work, we report synthesis of Cu, Pt and Pd doped SnO_2 powders and their comparative CO gas sensing studies. Dopants were incorporated into SnO_2 nanostructures using chemical and impregnation methods by using urea and ammonia as precipitation agents. The synthesized samples were characterized using X-ray diffraction (XRD), Raman spectroscopy, Scanning electron microscopy (SEM) and High resolution transmission electron microscopy (HR-TEM). The presence of dopants within the SnO_2 nanostructures was evidenced from HR-TEM. Doped powders utilizing chemical methods with urea as precipitation agent presented higher sensitivities compared to the remaining, which is due to the formation of uniform and homogeneous particles resulted from the temperature assisted synthesis. The particle sizes of doped SnO_2 nanostructures were in the range of 40-100 nm. An enhanced sensitivity around 1783 was achieved with Cu doped SnO_2 when compared with two other dopants i.e., Pt (1200) and Pd: SnO_2(502). The high sensitivity of Cu: SnO_2 is due to formation of CuO and its excellent association and dissociation in the presence of CO with adsorbed atmospheric oxygen at sensor operation temperatures resulted in high conductance. Cu: SnO_2 may be an alternative and cost effective sensor for industrial applications.

Keywords: tin oxide pellets; doping; HRTEM analysis; CO; sensitivity

1. Introduction

The Gas leak detection is a manner of constructive testing of dangerous combustible gases [1]. Carbon monoxide (CO) is a toxic industrial hazard gas produced from the incomplete burning of all carbon-based fuels. Different kinds of materials including Metal Oxide Semiconductor (MOS) are employed for detecting CO [2–8]. As Wagner discovered [9], adsorbed atoms and molecules on the MOS surface influence its conductivity. Among the MOS materials available, SnO_2 is usually considered to be one of the best candidate for developing gas sensors due to its relatively low cost of production and adequate oxygen vacancies [10,11].

Commercially available SnO_2 gas sensors mainly are in the form of thick or thin films, or pellets [12,13]. However, pellets are more viable for gas sensors due to their high porosity and no substrate effects. Dopants in MOS materials improves the surface reactivity with atmospheric oxygen and subsequently the sensitivity by residing on the surface in the form of metal clusters or by modifying

the crystalline structure [14,15]. For gas sensing applications, the major catalytically active doping additives are noble metals (Pd, Pt, etc.), and transition metals (Cu, Fe, etc.) [16–18]. In general transition metals serve as "accelerators" of various processes [19] and noble metals serve as "catalysts" and also decreases the sensor operation temperature [20]. Platinum (Pt) and Palladium (Pd) are the most used dopants due to their chemical inertness and high work function (~5.8 and ~5.4 eV, respectively) than the band gap (3.6 eV) of SnO_2 [21–25]. In other hand, Copper (Cu) is the most used transition metal for doping due its comparable ionic radius as tin. Radii of Sn^{4+} and Cu^{2+} are around 0.71 and 0.72 Å, respectively [26]. Also the association of Cu with atmospheric oxygen and its dissociation with CO, at elevated temperatures improves the surface conductivity of the Cu doped SnO_2 pellets [27].

Different methods like flame spray [28], sol-gel [29], micro wave radiation [30], and wet chemical synthesis [31] are reported for the preparation of SnO_2 powders. Among others, wet chemical synthesis employing urea as precipitant agent requires a moderate temperature process (80-100^{0}C) which grants coarse powders with adequate characteristics to be used in gas sensing applications [32]. In this work, SnO_2 pellets doped Cu, Pt and Pd, were synthesized by wet chemical synthesis using urea and ammonia as a precipitation agents. Ammonia was employed to observe the effect of precipitation agent in the particle size. Additionally, two methods were employed for incorporation dopants, Cu, Pt and Pd; namely, chemical doping and impregnation methods. Cu doped SnO_2 pellets show excellent gas response to CO as comparison Pt and Pd doped SnO_2 pellets in both doping methods. Simultaneously, the structural, morphological characterizations and their corresponding calculations provide us a clear and deep perception of the dopant effects on the sensing properties of SnO_2. Our assertion can demonstrate a viable way for understanding the effect of dopants on the SnO_2 gas sensors.

2. Materials and Methods

2.1 Preparation of former pure SnO_2 powders using urea and ammonia

Feedstock solution was prepared by mixing 0.4M aqueous tin chloride pentahydrate ($SnCl_4 \bullet 5H_2O$; J. T. BAKER) and urea (CH_4N_2O; Sigma Aldrich) in 1:2 ratio. Later the mixed solution was vigorously stirred and heated until the solution temperature reaches around 93±5°C. Unlike former case (urea), for precipitation agent, ammonia (NH_4OH; Sigma Aldrich), it was added drop by drop to 0.4M aqueous $SnCl_4 \bullet 5H_2O$ until the pH of the solution reaches 12. The resultant precipitates in both cases were centrifuged at 400 rpm for 1h using ROTINA-420R centrifuge and the obtained pastes were dried at 100 °C for 24h to eliminate the remaining solvents. Finally, the dried powders were calcined in a furnace at 800 °C for 2 h to obtain pure SnO_2 powders. All the synthesis conditions were studied, optimized and reported in our previous works [33,34].

2.2 Preparation of chemical doped SnO_2 powders

1 wt % aqueous $CuCl_2$ (Sigma Aldrich) was added to the previously prepared feed stock solution (0.4M aqueous $SnCl_4 \bullet 5H_2O$ and CH_4N_2O in 1:2 ratio). Later similar procedure as explain in section 2.1 is followed to obtain Cu doped SnO_2 powders (Cu: SnO_2) utilizing urea and ammonia precipitation agents. Similarly, Pt: SnO_2 and Pd: SnO_2 powders utilizing $PtCl_2$ and $PdCl_2$, respectively were obtained.

2.3 Preparation of impregnated SnO_2 powders

Primarily, 1g each of previously obtained (refer section 2.1) pure SnO_2 powders utilizing precipitation agent's urea and ammonia were considered. Subsequently, these powders were impregnated with 1 wt % aqueous solutions of dopant chlorides, $CuCl_2$, $PtCl_2$ and $PdCl_2$ (Sigma Aldrich), separately. All the impregnated powders were annealed at 350 °C for 2 h in air to remove the residual species. A resume of all the obtained samples by different doping methods and precipitation agents were listed in Table 1. Pellets were manufactured from all the obtained Cu, Pt and Pd doped SnO_2 powders by using a manual pressing machine. The optimal pressing conditions, after several trials, were 16 tons during 90 min.

Peer-reviewed version available at Sensors 2017, 17, , 1011; doi:10.3390/s17051011

Table 1. List of samples with their corresponding doping methods and precipitation agents employed.

Name of the sample	Doping method	Precipitation agent	Dopant
Cu: SnO_2_U_Chem	Chemical doping	Urea	Cu
Cu: SnO_2_A_Chem	Chemical doping	Ammonia	
Cu: SnO_2_U_Impe	Impregnation	Urea	
Cu: SnO_2_A_Impe	Impregnation	Ammonia	
Pt: SnO_2_U_Chem	Chemical doping	Urea	Pt
Pt: SnO_2_A_Chem	Chemical doping	Ammonia	
Pt: SnO_2_U_Impe	Impregnation	Urea	
Pt: SnO_2_A_Impe	Impregnation	Ammonia	
Pd: SnO_2_U_Chem	Chemical doping	Urea	Pd
Pd: SnO_2_A_Chem	Chemical doping	Ammonia	
Pd: SnO_2_U_Impe	Impregnation	Urea	
Pd: SnO_2_A_Impe	Impregnation	Ammonia	

2.4 Characterization

X-Ray diffraction analysis using a PANalytical diffractometer with CuKα at 20 mA and 40 KV was carried out to identify the phase compound, crystallite size, lattice parameters and the crystalline structure of the doped SnO_2 powders. Raman scattering spectroscopy of pure and doped SnO_2 powders were analysed by using 532 nm laser beams and detecting scattering signals by thermoelectrically cooled charge coupled detector.

Scanning electron microscope (SEM), by using an AURIGA equipment, was employed to examine the morphological characteristics and the particle size of the calcined agglomerates. Additionally, SEM was also employed to analyse the surface morphological characteristics of all synthesized powders. High Resolution Transmission Electron Microscope (HRTEM JEM-ARF 200F) was employed to mainly identify the dopants, additionally; crystallite size, crystal planes and the lattice spacing between the SnO_2 crystal planes were estimated.

For measuring CO sensing measurements, pure silver ohmic contacts were deposited on the pellets surface by the thermal evaporation technique. The experimental setup for measuring the electrical resistance of the pellets is shown in supplementary Figure S1. The measurements were made at three different operating temperatures, namely, 100, 200, and 300 °C. Lower operation temperatures (< 100 °C) do not lead to conductance changes. The conductance changes were registered by using a Keithley 2001 multimeter. For controlling the partial pressure in the chamber a TM20 Leybold detector was used. The sensitivity of the pellets, S = Rair/ Rgas, was obtained by calculating the electrical conductance ratio from the measured resistance in air, Rair, and in the presence of different concentrations of CO, 1, 5, 50, 100, 200 and 300 ppm, Rgas.

3. Results

3.1 X-ray diffraction analysis

In this work, doped SnO_2 nano crystals were synthesized under various conditions such as different precipitation agents, dopants and doping methods. Figures 1a-c depicts the XRD patterns obtained for Cu, Pt and Pd: SnO_2 powders respectively in comparison with pure SnO_2 XRD patterns. Irrespective of the precipitation agent and doping method, it is evident from Figures 1a-c that all the doped-SnO_2 powders exhibit the tetragonal rutile phase of SnO and SnO_2, simultaneously according to the JCPDS cards 06-0395 and 77-0450, respectively [35]. Whereas, undoped powders demonstrate pure SnO_2 peaks, no additional phases of SnO_2 were found (Figures 1a-c). Therefore, the presence of SnO and SnO_2 simultaneously for all doped powders concludes that the dopants reduces the SnO_2

crystallinity and inhibits the further oxidation of the SnO to SnO_2, the intergrowth mechanisms may occur at 800 °C thermal oxidizing temperature [36].

No additional peaks corresponding to Cu, Pt and Pd are found, which confirms the incorporation of all dopants into the SnO_2 crystal lattice in all the doping cases. An upshift and additional peaks were observed in all the doped powders which is corroborated to the decrease in the SnO_2 crystal quality, these discrepancies are much higher for Pt and Pd: SnO_2 as compared to Cu: SnO_2 powders. The amount of crystal discrepancies is proportional to the ionic radii of the dopants (ionic radii of Sn^{+2}, Cu^{+2}, Pt^{+2} and Pd^{+2} are 0.71, 0.73, 0.80 and 0.86 Å, respectively) [26,27].

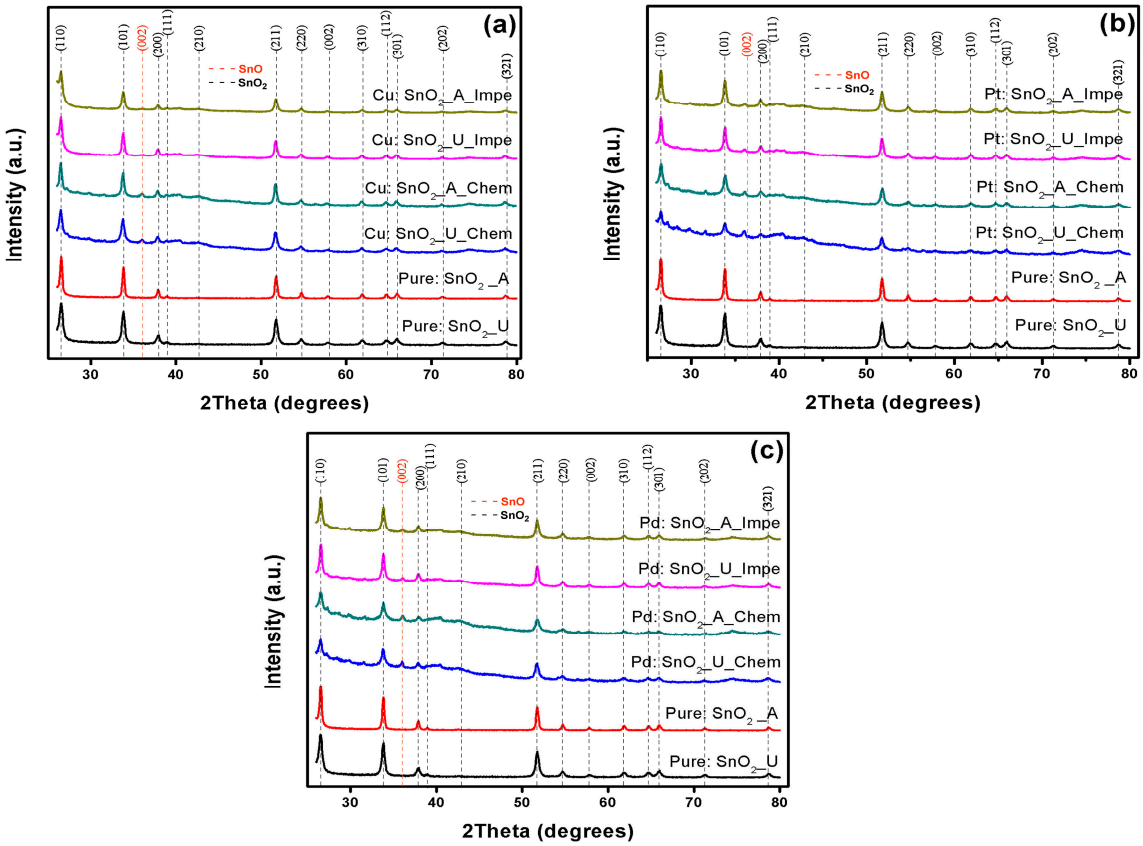

Figure 1. XRD patterns of (a) Cu: SnO_2; (b) Pt: SnO_2; and (c) Pd: SnO_2 powders for different precipitation agents and doping methods.

Figures 2a-c shows the shift in the SnO_2 preferential orientation plane (110) of Cu, Pt and Pd: SnO_2 samples, respectively. Irrespective of the dopant (Cu, Pt and Pd) utilized, chemically doped powders shift slightly to a higher angle compared to impregnated powders. A left shift with peak broadening was observed for Cu: SnO_2 powders (Figure 2a), on the contrary a right shift is evidenced for Pt: SnO_2 and Pd: SnO_2 (Figures 2b and 2c). This clearly evidences that the incorporated dopants developed a strain in SnO_2 crystal which resulted in a planar stress, shift to a lower angle for Cu: SnO_2 powders corresponds to compressive stress and to higher angle for Pt, Pd: SnO_2 powders represents tensile stress [26,27].

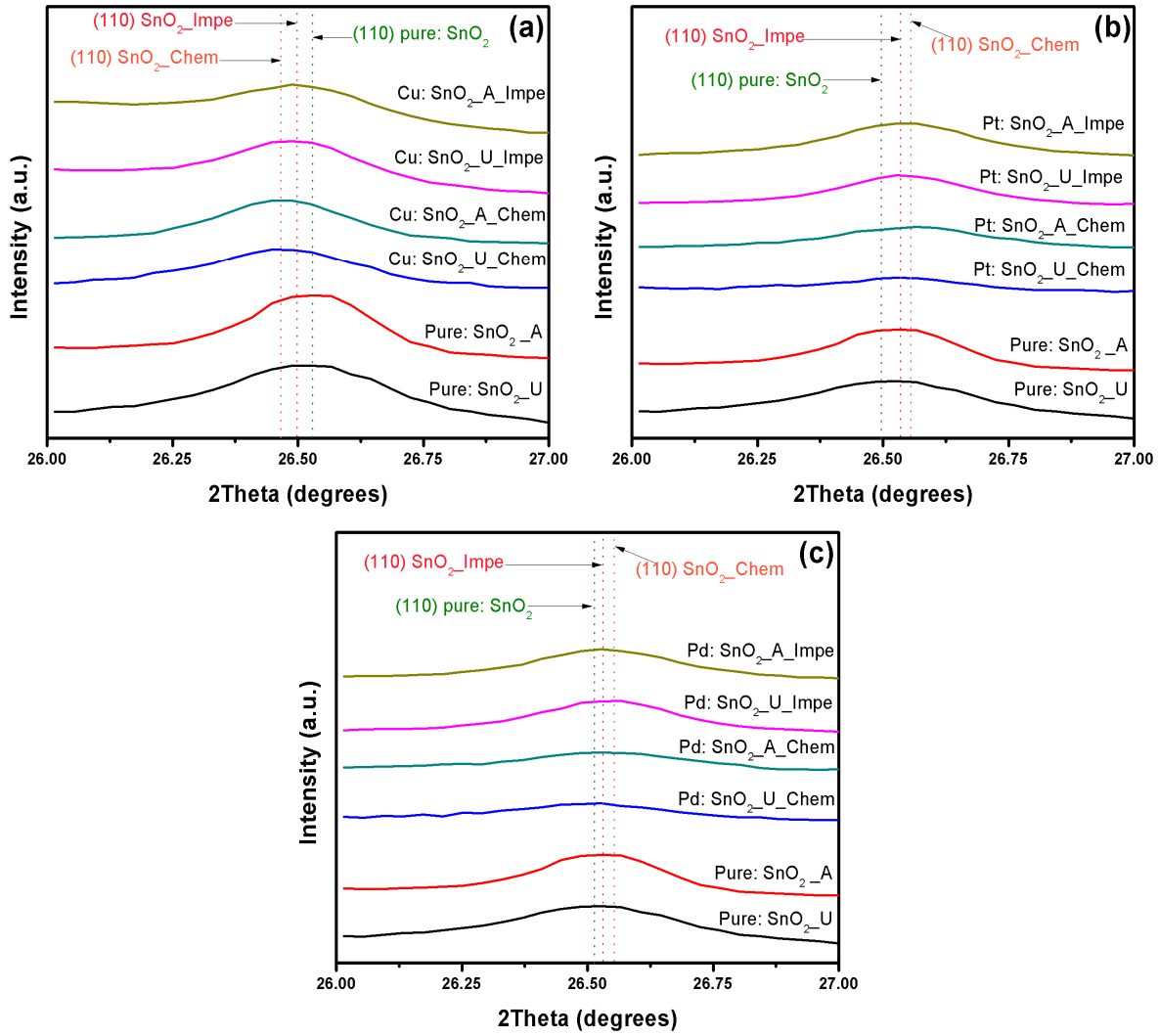

Figure 2. (110) plane shift and peak broadening of (a) Cu: SnO_2; (b) Pt: SnO_2; and (c) Pd: SnO_2 powders for different precipitation agents and doping methods.

In order to ascertain the effect of dopants (Cu, Pt and Pd) on the structural characteristics, crystallite size (D) [37], crystal volume(V) [38] and porosity (P) [39] are calculated from equations (1-5) and reported in Table 2.

$$D = \frac{0.89\lambda}{\beta \mathrm{Cos}\theta} \quad (1)$$

$$V = a^2 c \quad (2)$$

$$P = \left(1 - \frac{\rho_a}{\rho_x}\right) \times 100\% \quad (3)$$

$$\rho_a = \frac{m}{v} \quad (4)$$

$$\rho_x = \frac{nM}{NV} \quad (5)$$

whereas λ is the wavelength of incident X-ray (λ = 0.15418 nm), β is the full width half maximum (FWHM) intensity, θ is the Bragg's diffraction angle in radians, a and c are lattice parameters, m and v are mass and volume of the samples, n is number of molecules per unit cell, M is molecular weight and N is Avogadro's number.

Table 2. Crystallite size (D); Volume of the crystal (V); and Porosity (P) of the Cu, Pt and Pd-SnO_2 nano crystals.

Sample name	D (nm)	V (10^{-24} cm^3)	P (%)
SnO_2_U	26.2758	71.4083	32.30277
SnO_2_A	30.0292	71.643	32.42236
Cu: SnO_2_U_Chem	21.1751	71.6685	58.35864
Cu: SnO_2_A_Chem	21.028	71.7153	58.46007
Cu: SnO_2_U_Impe	22.1751	71.724	58.46007
Cu: SnO_2_A_Impe	22.028	71.7536	58.68875
Pt: SnO_2_U_Chem	35.0255	71.7671	64.62565
Pt: SnO_2_A_Chem	35.0267	71.7869	64.72664
Pt: SnO_2_U_Impe	33.0283	71.8223	64.75372
Pt: SnO_2_A_Impe	33.0284	71.8509	64.80217
Pd: SnO_2_U_Chem	42.0347	72.0279	73.01781
Pd: SnO_2_A_Chem	42.0377	72.0396	73.03034
Pd: SnO_2_U_Impe	40.0286	72.0396	73.04474
Pd: SnO_2_A_Impe	40.0291	72.2155	73.16012

From Table 2 it can be observed that, for Cu: SnO_2 powders, the crystallite sized decreased (a left shift, compressed stress; Figure 2) from 26 to 21 nm, whereas for Pt and Pd: SnO_2 powders crystallite size increased (a right shift, tensile stress; Figure 2) from 26 to ~ 35 and 42 nm, respectively. These changes in crystallite changes are in good agreement with the peak shifts observed from Figure 2. SnO_2 crystallite size of chemically doped powders decrease more with Cu doping and increases more for Pt and Pd dopants, compared to impregnated powders. The higher ionic radii of Pt and Pd compared to Sn and higher results in a tensile stress and increase in SnO_2 crystallite size for Pt, Pd: SnO_2 powders [40]. Presence of Cu inhibited further SnO_2 growth and decreased the crystallite size whereas seeing of compressed stress for Cu: SnO_2 powders are a puzzle. A linear relation is noticed between the volume of unit cell and porosity and is apparent because doping with an atom with higher ionic radius increases the volume of the unit cell and subsequently porosity. No significant effects of precipitation agent (urea/ammonia) on structural properties were observed.

3.2 Raman analysis

To confirm the effect of precipitation agent and doping method on the SnO_2 nanoparticles growth, Raman spectroscopy measurements were carried out. It is well known that SnO_2 has a tetragonal structure having 6 atoms (2 Sn and 4 O) per unit cell [41]. The 6-unit cell atoms give a total of 18 branches for the vibrational modes in the first Brillouin zone. The mechanical representation of the normal vibration modes, all the vibrational modes of SnO_2 with corresponding Raman shift peaks were also widely known and reported by various authors [42–44]. Table 3 resumes different frequencies of the optical modes of SnO_2, with corresponding vibrational directions.

Table 3. Raman, IR and other vibrational modes of SnO_2.

Modes	Notation	Direction of vibration with respect to c-axis	Raman shift (cm^{-1})
Raman active	A_{1g}	Perpendicular	638
	B_{1g}	Perpendicular	100
	B_{2g}	Perpendicular	782
	E_g	Parallel	476
IR active	A_{2u}	Parallel	705
	E_u	Perpendicular	244
Silent	A_{2g}	Perpendicular	398
	B_{1u}	Parallel	140

The Raman spectra of Cu, Pt and Pd: SnO_2 synthesized by different doping methods are shown in Figures 3a and 3b. One IR active and three raman active modes were observed at 255.2, 482.8, 637.6 and 779.2 cm^{-1}, corresponding to the E_u, E_g, A_{1g}, and B_{2g} vibration modes of SnO_2, respectively, corresponding to the rutile bulk SnO_2 [45]. The intensity of the Raman peaks denotes the amount of extraction and compression of Sn-O bonds in the lattice [46]. It is interesting to note that the Cu doping decreases the intensities of Raman peaks (Figure 3a) which is corroborated to the Sn-O disorders arise due to Cu incorporation, in the SnO_2 lattice.

From Figure 3a, it can also be observed that, the intensities of A_{1g} Raman peak were very less for powders synthesized with ammonia as precipitation agent. The rate of decrease in A_{1g} peak intensity is higher for chemically doped powders than the impregnated ones. No peak shifts were observed from the Raman spectra, the minimum amount of doping percentage for observing a peak shift in Raman spectra was around 3 wt % [43–45].

Figure 3b shows a comparison of the Raman spectra of chemically doped Cu, Pt and Pd: SnO_2 with urea as precipitation agent. Cu: SnO_2 doped powders present higher intensities than Pt and Pd: SnO_2 powders which is correlated to the ionic radii of the dopant ions. As the Pd has higher ionic radius compared to Pt and Cu, it causes higher Sn-O disorders in the lattice which makes the intensities of Pd: SnO_2 powders to diminish.

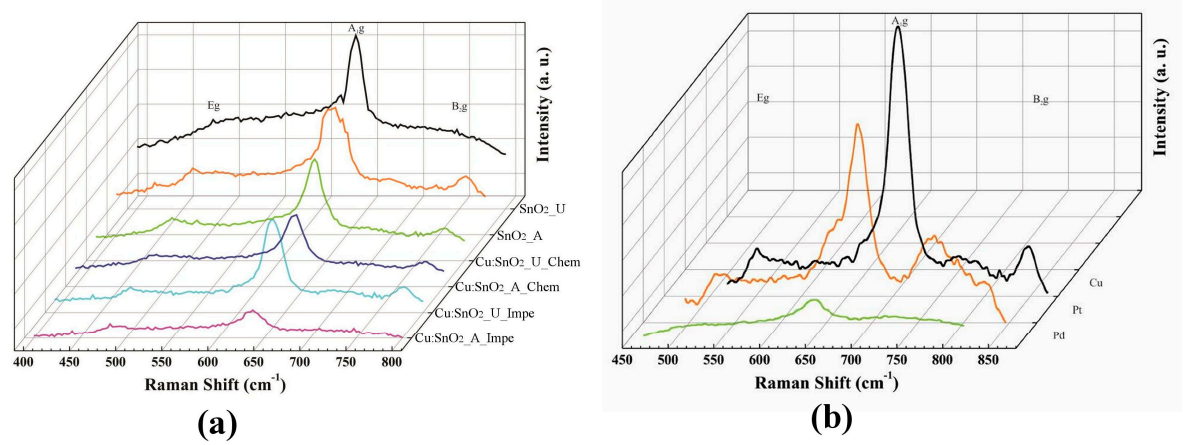

Figure 3. Raman spectra of the (a) Cu-SnO_2 with different doping methods; and (b) chemically doped Cu, Pt and Pd: SnO_2 with urea as precipitation agent.

3.3 SEM analysis

SEM was employed to further examine and interpret the morphologies and structures of the powders with respect to the precipitation agent and dopant methods. Figures 4a–d shows the representative SEM images of Cu: SnO_2_U_Chem, Cu: SnO_2_A_Chem, Cu: SnO_2_U_Impe, Cu: SnO_2_A_Impe, respectively. The average diameters of Cu: SnO_2 nano particles observed are in the range 25-35 nm.

From Figure 4, powders that are chemically doped (Figures 4a and 4b) shows a contact area between particles, which are the necks between grains. The additives which are added during the synthesis process are incorporated in the lattice of metal oxide, which further inhibits the grain size [47] and promotes coalescence during the heat treatment. This later coalescence leads to the formation of necks between the grains [48], which in turn influence the bulk conductivity and the thickness of the space charge region. On the other hand, impregnated powders (Figures 4c and 4d) shows only an agglomeration between the particles, the additives which are impregnated on the thermally treated SnO_2 powders which does not promote the coalescence.

From Figures 4b and 4d, it is also evident that, larger crystals around 200-600 nm additional to the SnO_2 nano particles, were observed for the powders with ammonia as precipitation agent. The formation of larger crystals is due to the rapid precipitation at room temperature. In case of powders precipitated using urea (Figures 4a and 4c), the elevated temperature around 90 °C utilized, for

Peer-reviewed version available at Sensors 2017, 17, , 1011; doi:10.3390/s17051011

decomposing urea, also resulted in homogenous precipitation [49]. This resulted in a uniform particle size and similar behaviour was noticed for the Pt and Pd: SnO_2 powders (Figure 5).

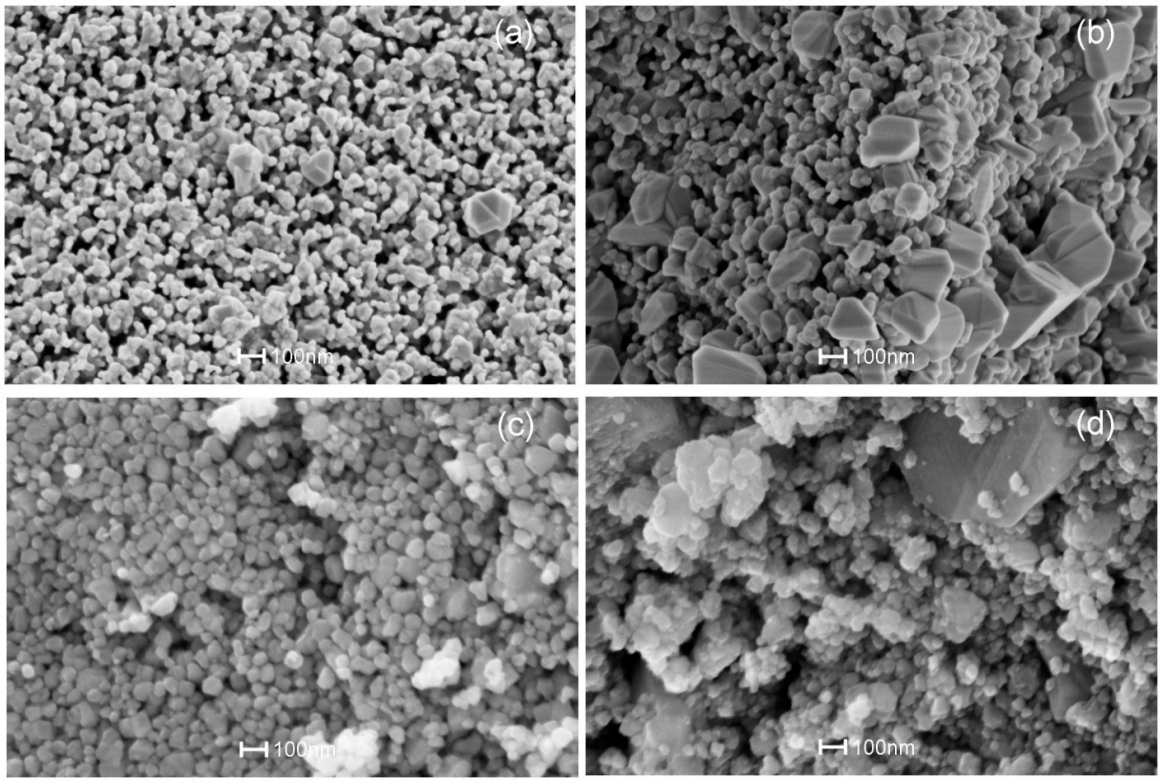

Figure 4. SEM images of (a) Cu: SnO_2_U_Chem; (b) Cu: SnO_2_A_Chem; (c) Cu: SnO_2_U_Impe; and (d) Cu: SnO_2_A_Impe.

Figure 5a-d shows the representative SEM images of Pt: SnO_2 and Pd: SnO_2 powders obtained by chemical doping and impregnation, respectively. As like Cu: SnO_2 powders, Pt and Pd: SnO_2 powders also shows necks between the grains, for chemically doped ones (Figures 5a and 5c). The average diameters of Pt and Pd: SnO_2 nano particles observed are around 35 and 45 nm respectively. The particles size increased very slightly around 10nm for Pt and Pd compared to Cu doped powders. From Figures 4 and 5, we can conclude that the chemically doped powders are favourable to promote gas sensing because the conductivity increases due to the formation of necks between the grains [50].

Porosity is another important factor that affects the sensitivity [51]. It has already been reported [52,53] that, the SnO_2 sensitivity increases with respect to the porosity with different additives. An increment in the surface porosity will increase the active surface area which allows the sensing gas to diffuse into the pellet pores [54]. To observe the pellet surface porosity, powders obtained by chemically doped Cu: SnO_2 were observed in SEM at a lower magnification and the results are shown in Figure 6. The porous surface has morphology of mesh-like due to the smaller particle size and formation of necks between the particles.

Peer-reviewed version available at Sensors 2017, 17, , 1011; doi:10.3390/s17051011

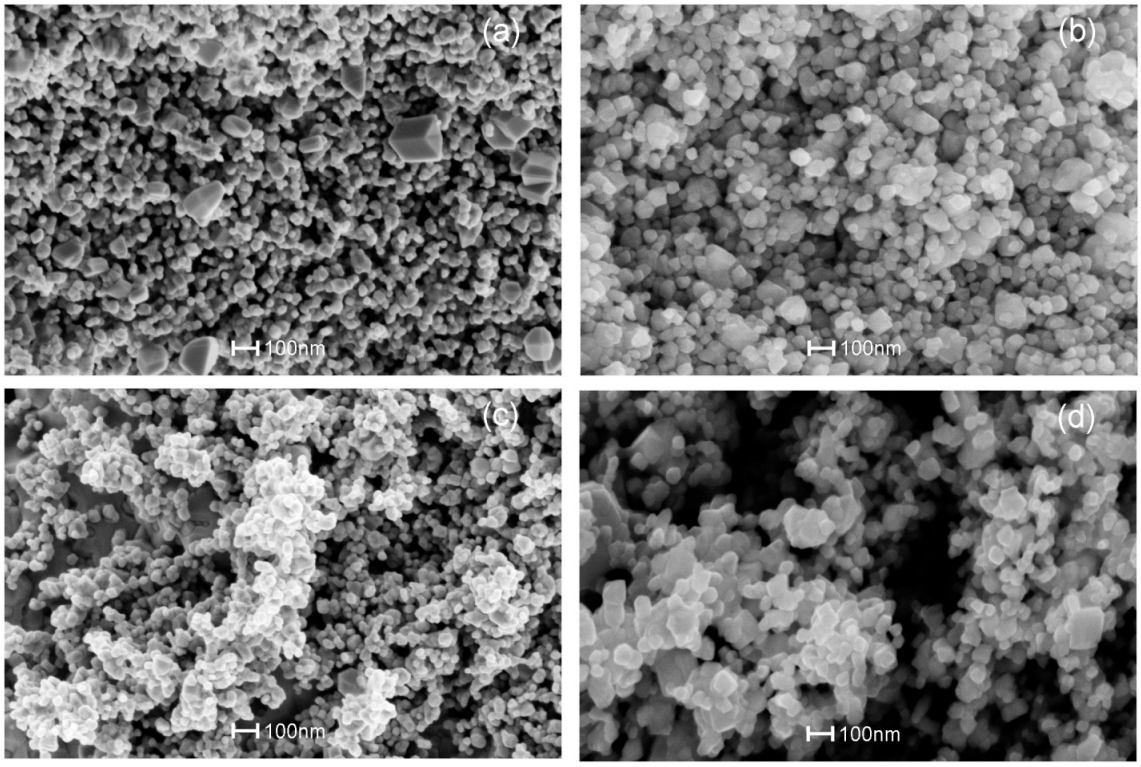

Figure 5. SEM images of (a) Pt: SnO_2_U_Chem; (b) Pt: SnO_2_A_Chem; (c) Pd: SnO_2_U_Chem; and (d) Pd: SnO_2_A_Chem.

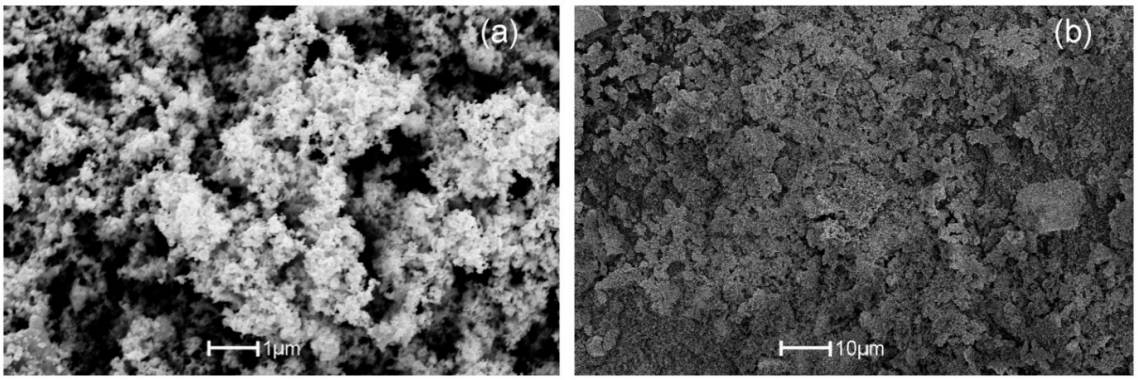

Figure 6. SEM images of chemically doped Cu: SnO_2 at magnification of (a) 1μm; and (b) 10μm.

3.4. HRTEM analysis

It was evident from the SEM analysis that the powders synthesized with precipitation agent urea have a uniform particle size than others. To obtain more-detailed information about the crystal structure of Cu, Pt and Pd doped SnO_2 particles were analysed by HRTEM. Figure 7 shows the Cu: SnO_2 particles prepared by chemically doping (a) and impregnation (b). The powders are composed of agglomerated nanometric crystals around 25-30 nm, which is in good agreement with the XRD results.

A magnification view of Figures 7a and 7b are shown in Figures 7c and 7d and their corresponding reconstructed images are shown in Figures 7e and 7f, respectively. The insets in Figures 7e and 7f are the corresponding selected-area electron diffraction (SAED) patterns. The difference in the doping method is remarkable (chemically doped/ impregnated). In the case of the chemically doped sample, all the atomic planes are well defined and correspond to SnO_2 crystal (Figure 7c) and its surface is free from any dopants unlike for impregnated powders (Figure 7d). The *d*-spacing's measured from SAED are in good agreement with those of the (110) plane of cassiterite

Peer-reviewed version available at Sensors 2017, 17, , 1011; doi:10.3390/s17051011

SnO_2 (JCPDS Card 77-0450 card) [35], corresponding to the tetragonal crystal structure (space group = *P42/mnm*).

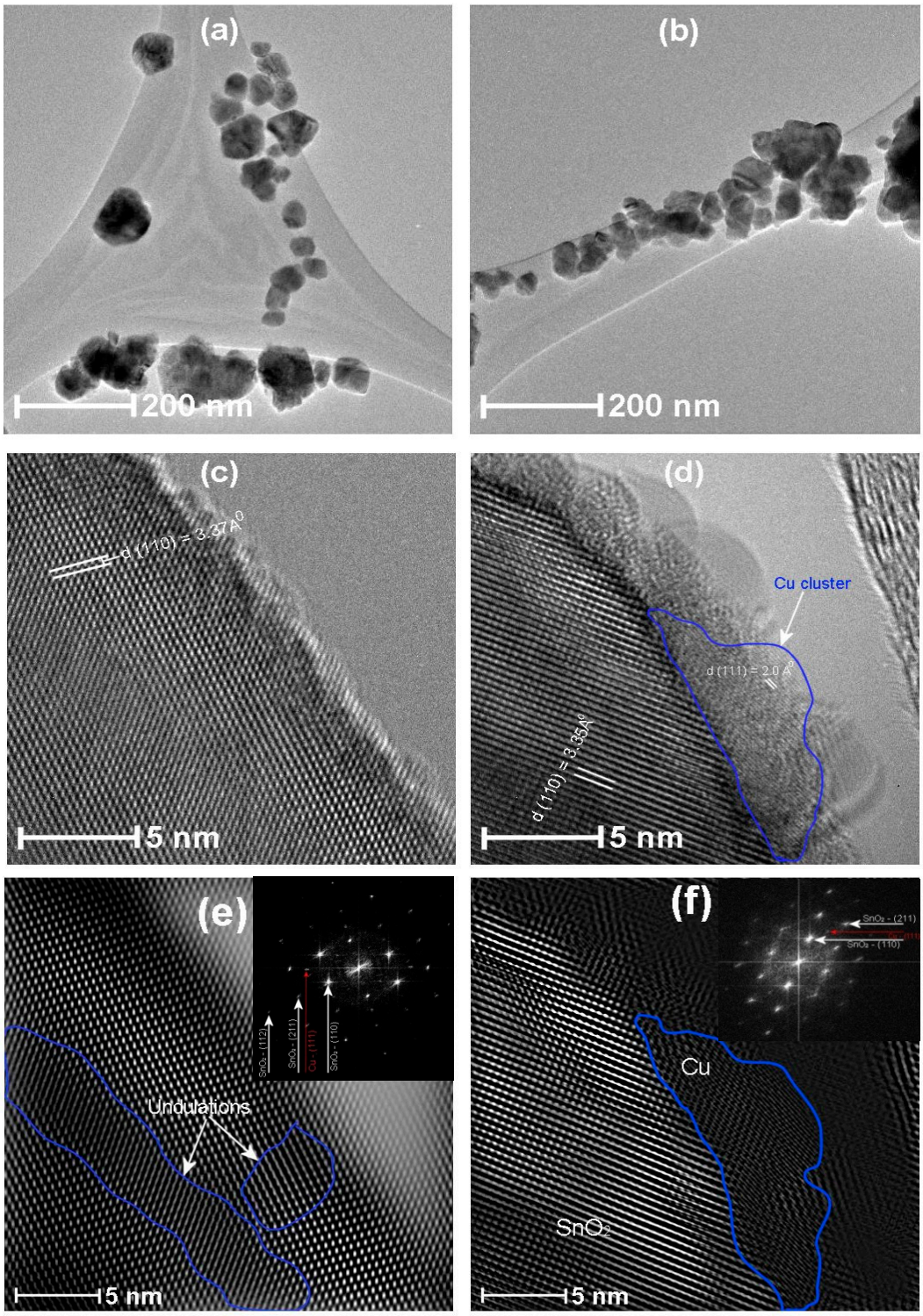

Figure 7. HRTEM images of Cu: SnO_2 prepared by method (a) Cu: SnO_2_U_Chem; (b) Cu: SnO_2_U_Impe; a higher magnification of surface of SnO_2 crystal surface (c) Cu: SnO_2_U_Chem; (d) Cu: SnO_2_U_Impe; (e) reconstructed HRTEM after masking of (c); inset: the corresponding SAED pattern, and (f) reconstructed HRTEM image after masking of (d); inset: the corresponding SAED pattern.

Cu doping localized on the surface of the SnO_2 particle was observed for the impregnated powders (Figures 7d and 7f), marked in blue region. Also, no defects were founded in the SnO_2 crystal. The inter-plane distance measured for the copper particle corresponds (111) plane of cubic Cu (JCPDS Card 00-004-0836) [55], which confirms that the cluster formation of the dopants takes place on the surface of the SnO_2, which assures the possibility of spill over mechanism in the gas sensing properties.

Contrarily, for chemically doped powders, no clusters of dopants were observed on the surface but the surface undulations produced by doping were observed and marked in Figure 7e, highlighted in blue regions. Therefore, while using the chemical doping method, the dopants are incorporated into the SnO_2 lattice. Moreover, the (110) inter-plane distance estimated to be 3.35, 3.37 and 3.36 Å for undoped, chemically doped and impregnated powders, respectively. This increase in the lattice parameter suggests an increase of the unit cell volume for the doped powders, which is a cogent evidence for Cu insertion in the host (SnO_2) matrix. The estimated lattice spacing values from the HRTEM are in consistent with the calculated XRD data. A comparison of calculated d-spacing values for all the dopants and doping methods are tabulated in Table 4. Change in the lattice spacing is slightly higher in chemically doped powders which is consistent with the higher left shift in the (110) diffraction peak (Figure 2).

Table 4. A comparison of estimated d-spacing values for all the dopants and doping methods.

Dopant	SnO_2 - d (110) in Å					
	Urea	Ammonia	Chemically doped		Impregnated powders	
			Urea	Ammonia	Urea	Ammonia
Undoped	3.35853	3.35492	--	--	--	--
Cu	--	--	3.3732	3.36927	3.3682	3.3927
Pt	--	--	3.39422	3.38839	3.3801	3.35427
Pd	--	--	3.41855	3.40501	3.40697	3.35706

Figure 8a shows surface of the Cu: SnO_2 crystal divided in regions I and II, with their corresponding reconstructed (Figures 8b and 8c) patterns. Figures 8b and 8c evidences the stacking faults (marked with red arrows) in SnO_2 lattice, which are attributed due to the Cu doping.

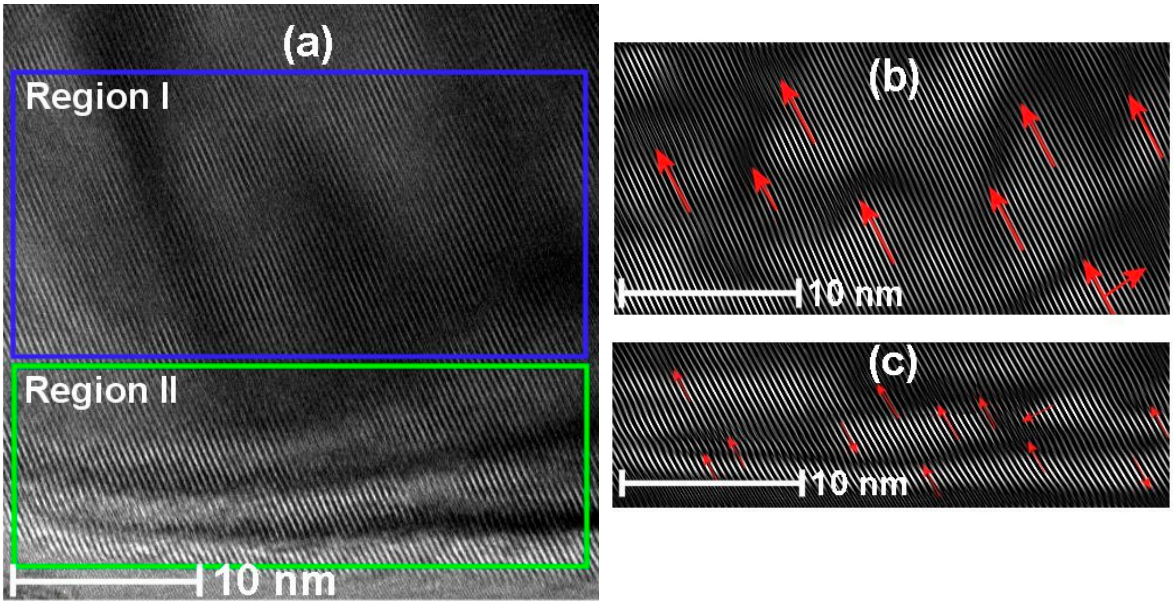

Figure 8. HRTEM images of chemically doped Cu: SnO_2 prepared using urea as precipitation agent (a) surface of the SnO_2 crystal with stacking faults; (b) reconstructed image of Region I; and (c) reconstructed image of Region II.

Peer-reviewed version available at Sensors 2017, 17, , 1011; doi:10.3390/s17051011

In "Region I" from Figure 8 these faults were consistently observed on all surfaces of chemically doped SnO_2 powders. The numbers of defects produced were more in case of Pt and Pd than in Cu, which is due to the higher ionic radii for Pt and Pd.

Figures 9a and 9c shows the defects produced for the chemically doped SnO_2 powders with Pt and Pd, respectively. FFT reconstructed images of the Figures 9a and 9c are shown in the Figures 9b and 9d, respectively. For Pt, doped SnO_2 powders the stacking faults obtained are in the (110) plane surface, which are marked with red arrows. Whereas, in case of Pd: SnO_2 powders, as shown in the Figure 9d, the stacking faults or defects obtained on the {221} facets of SnO_2 projected from (110) plane. The {221} is a typical facet of SnO_2 and can be described as combination of (001) and (110) steps [56].

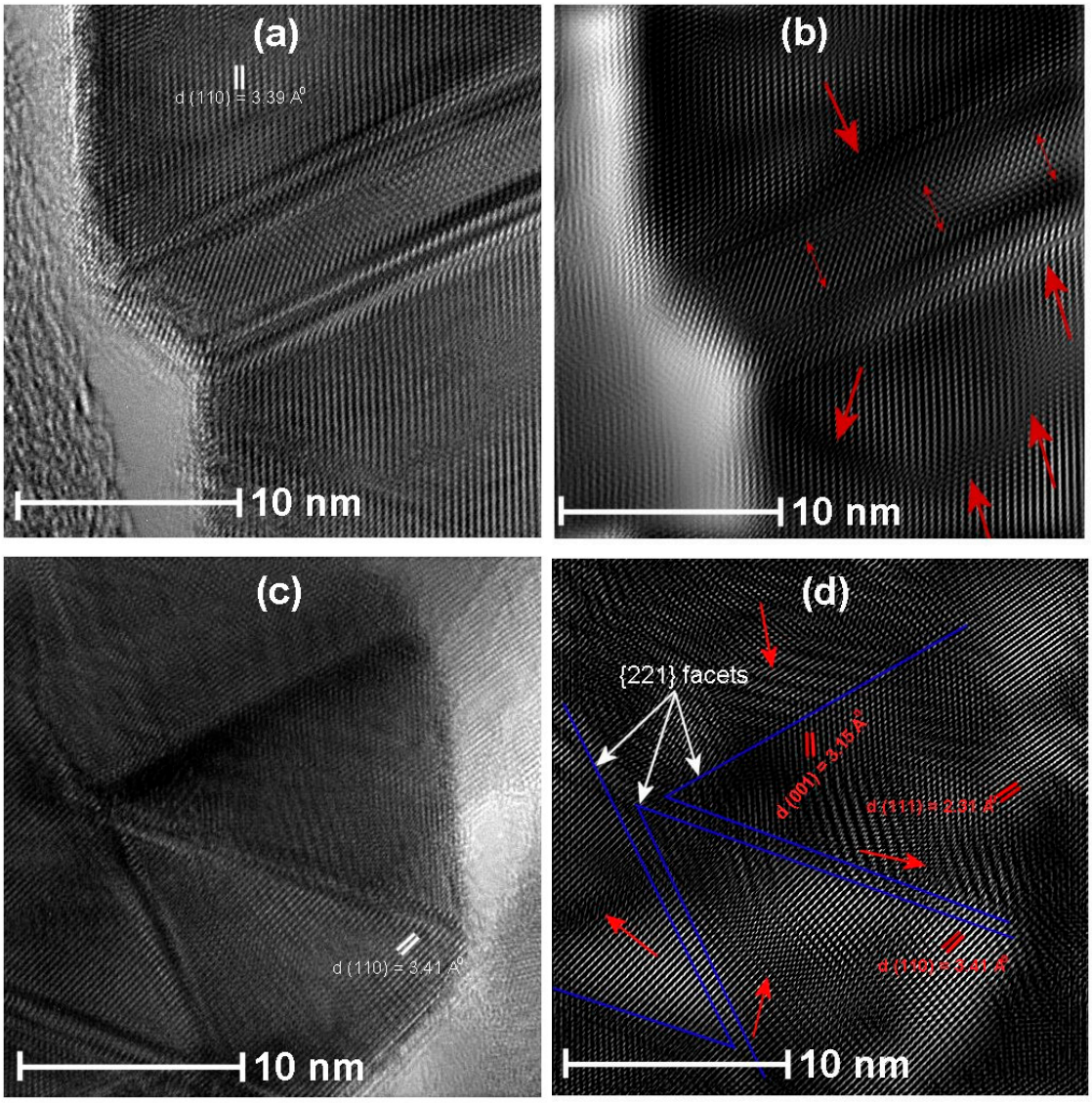

Figure 9. HRTEM images of chemically doped (a) Pt: SnO_2; (c) Pd: SnO_2 prepared using urea as precipitation agent; (b) and (d) are reconstructed HRTEM after masking of (a) and (c), respectively.

According Xiguang Han, et.al [56], {221} facets are very favourable for gas sensing properties. Further detailed chemical analysis regarding Pd: SnO_2 crystals is required to explain the reasons for the formation of {221} facets. The (110) inter-plane distance calculated was 3.39 and 3.41 Å for chemically doped Pt and Pd: SnO_2 powders, respectively. The presence of dislocations and stacking faults observed in HRTEM analysis agrees with the Raman bands of Cu, Pt and Pd doped SnO_2 powders, which show an asymmetric broadening A_{1g} Raman peak (Refer Figure 3b). The internal strain produced due to the doping leads to a downshift and broadening of the A_{1g} Raman peak [57]. Additionally, due to the stacking faults, the crystals obtained are with Sn enriched stoichiometry in addition to Sn-interstitials and oxygen vacancies [58]. Therefore, the increment in the [Sn]/ [O] ratio at the stacking fault causes electronic effects, which increases bulk conductivity and subsequently CO sensitivity.

3.5. CO sensing properties

CO gas sensing measurements were performed for the manufactured Cu, Pt and Pd doped SnO_2 pellets to taste their potential applications in chemical sensors. The top and cross sectional view of the gas sensor employed in this work are shown in Figures 10a and 10b respectively.

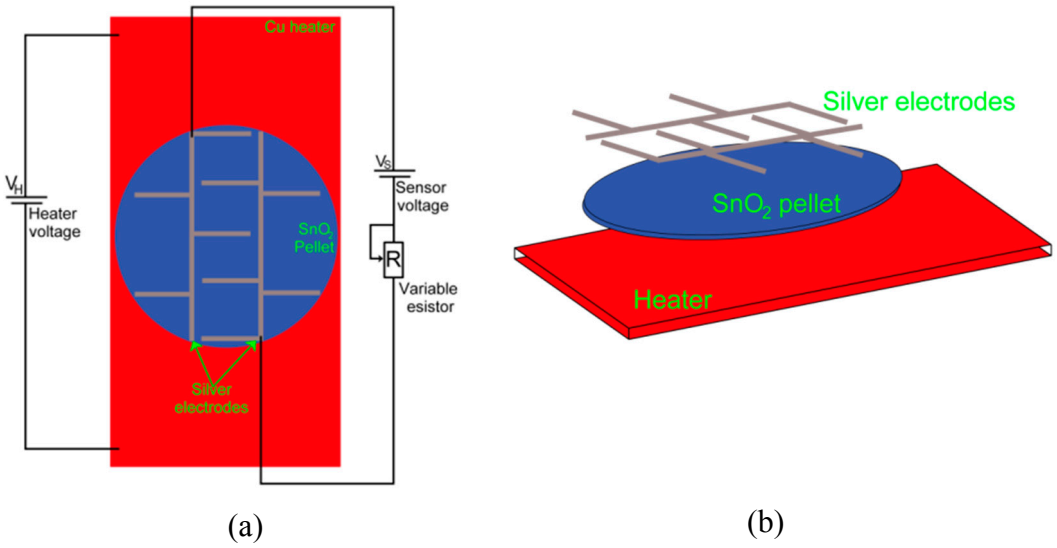

Figure 10. (a) Top view and (b) cross sectional view of SnO_2 sensor.

To study the effect of precipitation agent, dopants and doping method on the measuring temperature and CO gas concentration of our SnO_2 samples, the sensors response has been tested as a function of CO gas in the range of 1–300 ppm at 100, 200 and 300 °C temperatures. Figures 11a-d corresponds to the CO sensing properties of Cu: SnO_2_U_Chem, Cu: SnO_2_A_Chem, Cu: SnO_2_U_Impe and Cu: SnO_2_A_Impe, respectively. Table 5 resumes the highest sensitivities obtained at 300°C for 300ppm of CO gas concentration, for different dopants used, synthesis routes and doping methods. The undoped sensitivities are reported from our previous work [34].

Irrespective of dopants used, doping methods and synthesis routes employed, the sensitivities of doped SnO_2 pellets are higher than undoped SnO_2 (Table 5). From Figures 11a-d and Table 5, it can be observed that, irrespective of synthesis route and doping method employed, all the pellets sensitivity increases with an increment in the gas concentration and measuring temperature.

Also, Cu: SnO_2_U_Chem, Cu: SnO_2_A_Chem, Cu: SnO_2_U_Impe and Cu: SnO_2_A_Impe, exhibits a rapid increase of response to reach the maximum value of 1782, 1625, 975 and 1666 respectively at the measuring temperature of 300 °C. Chemically doped powders have a slight increase in sensing response when measured at 100 and 200 °C (refer insets of Figures 11a and 11b), whereas the impregnated powders shows an effective sensing response at the measuring temperature of 200 and 300 °C(Figures 11c and 11d). Finally, irrespective of doping method, pellets manufactured with urea as precipitation agent show higher sensitivities than powders utilizing

Preprints (www.preprints.org) | NOT PEER-REVIEWED | Posted: 4 April 2017 doi:10.20944/preprints201704.0014.v1

Peer-reviewed version available at Sensors 2017, 17, , 1011; doi:10.3390/s17051011

ammonia as precipitation agent (Table5). Even under low concentrations (1–50 ppm) and high concentrations (100–300 ppm), the response increases linearly with the CO concentration for all the measuring temperatures (Figures 12a and 12b insets).

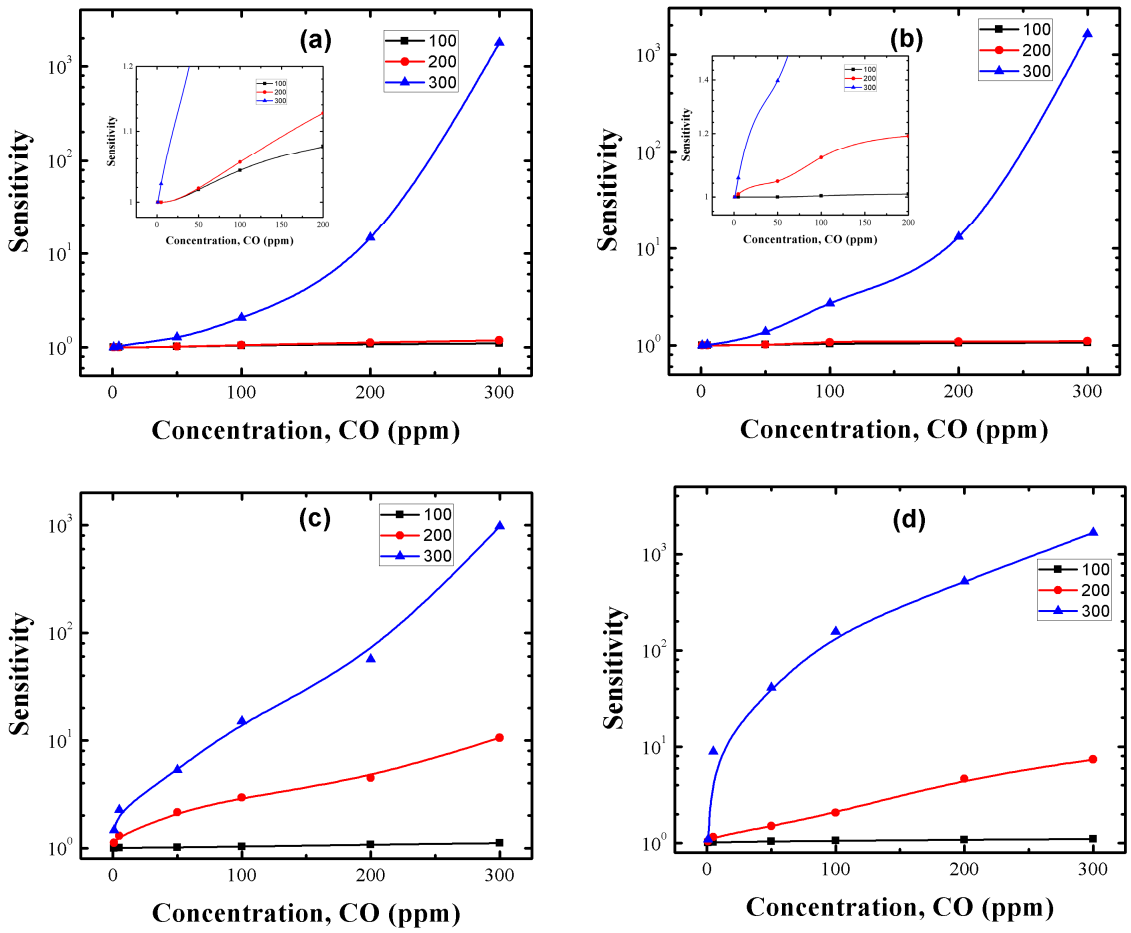

Figure 11. Sensitivity of (a) Cu: SnO_2_U_Chem; (b) Cu: SnO_2_A_Chem; (c) Cu: SnO_2_U_Impe; and (d) Cu: SnO_2_A_Impe.

Table 5. Sensitivities at 300°C for 300ppm of CO of the Cu, Pt and Pd doped SnO_2 pellets prepared by different methods.

	Undoped	Cu	Pt	Pd
U_Chem	12	-	-	-
A_Chem	10	-	-	-
U_Chem		1782.609	1200	502.5
A_Chem		1625	721.519	287.6405
U_Impe		1666.667	428.7234	245.4546
A_Impe		975.7412	387.3333	224.1485

To study the effect of the dopant type on the CO sensitivities, the sensor response of the Pt and Pd doped SnO_2 pellets were tested taking in consideration the different doping methods, results are reported in Figure 12. We can observe that, Pt and Pd doped pellets are in the sensitivity range of the Cu doped pellets. The sensitivities increase with respect to temperature and gas concentration for

both Pt and Pd doped samples. In a second hand, impregnated powders showed sensitivities at lower temperatures around 200 and 300 °C. Finally, the sensitivities of Pt doped samples are higher than Pd doped but is less compared to Cu doped samples. Chemically doped powders show higher sensitivities than the impregnated ones for all Cu, Pt and Pd: SnO_2powders (Table5).

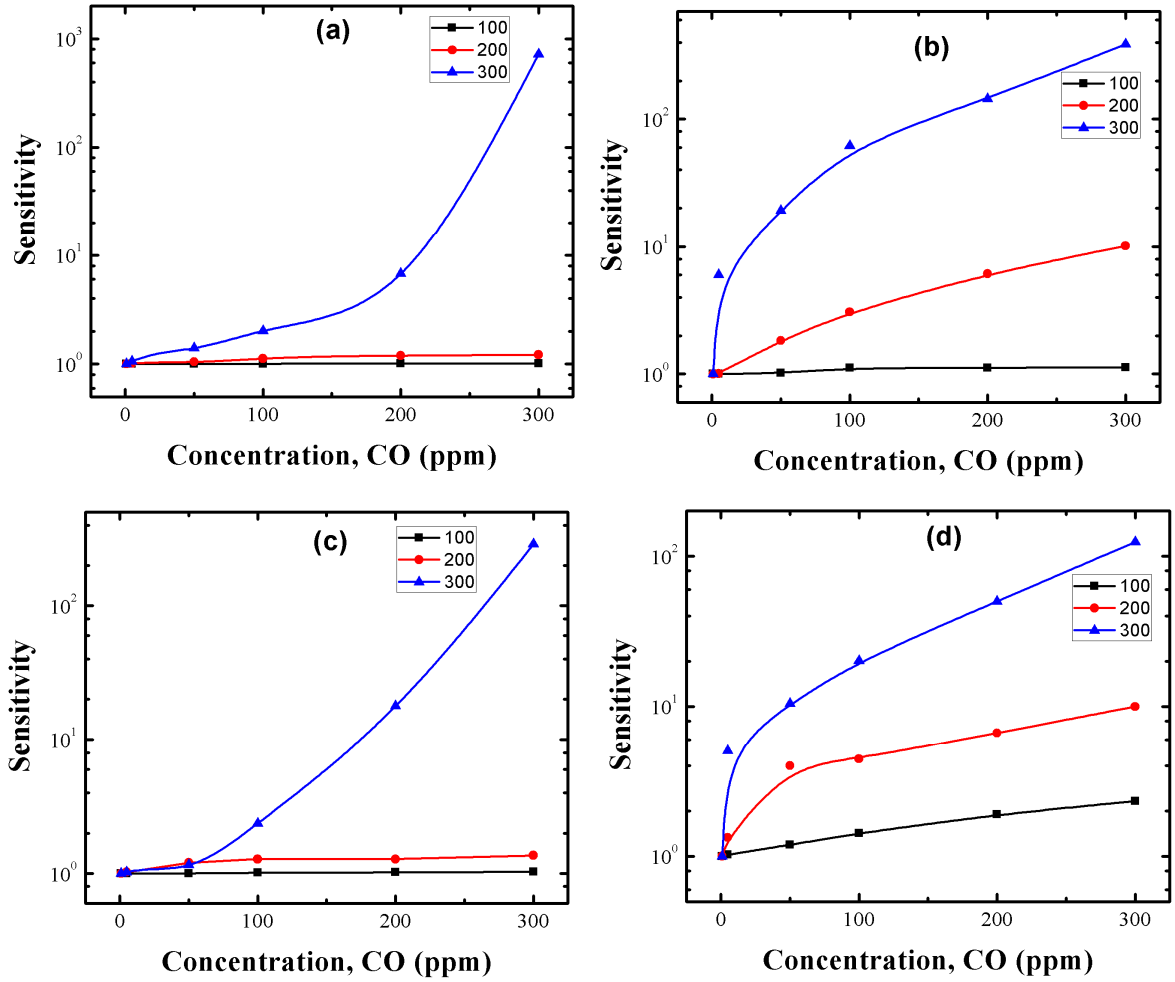

Figure 12. Sensitivity of (a) Pt: SnO_2_U_Chem; (b) Pt: SnO_2_A_Chem; (c) Pd: SnO_2_U_Chem; and (d) Pd: SnO_2_A_Chem.

Figure 13 resumes out the sensitivities of the Cu, Pt and Pd: SnO_2 pellets prepared by different doping methods and precipitation agents, measured at 300°C for 300ppm of CO. We can observe that the Cu (green bar) shows higher sensitivities that Pt (blue bar) and Pd (red bar) in each case. Sensitivity increases with respect to the measuring temperature and gas concentration. The detailed explanation of the above obtained results and their corresponding reasons will be discussed in upcoming section 3.6.

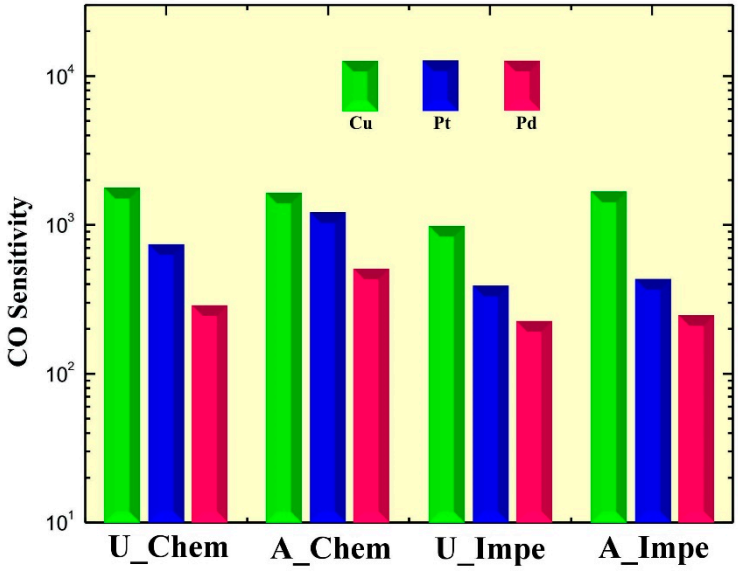

Figure 13. Precipitation agents (urea and ammonia); doping methods (chemically doped and impregnated) comparison of Cu, Pt and Pd: SnO_2 CO sensitivities of manufactured pellets.

4. Discussion

4.1. Gas sensing mechanism

Description of the oxygen adsorption on a metal oxide with a change in surface conductivity with respect to the CO is presented in Figure 14. As the temperature increase, atmospheric oxygen adsorbs on the SnO_2 surface due to its oxygen vacancies which results in the formation of a depletion region between adsorbed oxygen and SnO_2 surface (left column of Figure 14). Later, as the reducing gas interacts with the adsorbed oxygen and increase the conductivity which is measured as a sensor signal (right column of Figure 14).

A rise in the CO gas concentration leads to an increment in the number of reactions with the pellet surface, which in turn increases the magnitudes of conductivity and subsequently sensitivity. Also, the oxygen species adsorbed at higher temperatures above 300 °C, are atomic (O^-) which are more reactable, whereas the adsorbed oxygen at 100 and 200°C temperatures are in molecular form (O_2, O^{2-}) [59]. Therefore, sensitivity increases accordingly to the gas concentration and temperature which is in consistent with our results reported in Figures 11 and 12. From the SEM and HRTEM results obtained, it is evident that the structures obtained are non-spherical and porous, which provides an additional active sites to adsorb more oxygen species which increased the sensitivity [60]. Figure 15 indicates the difference between the contact area for a spherical and non-spherical contacts. For illustrative purposes, considering that the non-spherical structures formed as tetragonal (which is a typical phase of SnO_2), results in a different contacting form with different contact area.

As shown in Figure 15a, for spherical structures with point-to-point contacting consists of relatively less contact area compared to the tetragonal structures with the face-to-face contacting as shown in Figure 15b. When different tetragonal particles are exposed to air, oxygen adsorption between the face-to-face contact results in a less resistive depletion region between the adjacent particles compared to the point-to-point contact. The face-to-face contacting form of tetragonal particles enhances the surface-depletion control rather than grain boundary barrier control, which results in a higher sensitivity.

Preprints (www.preprints.org) | NOT PEER-REVIEWED | Posted: 4 April 2017 doi:10.20944/preprints201704.0014.v1

Peer-reviewed version available at Sensors 2017, 17, , 1011; doi:10.3390/s17051011

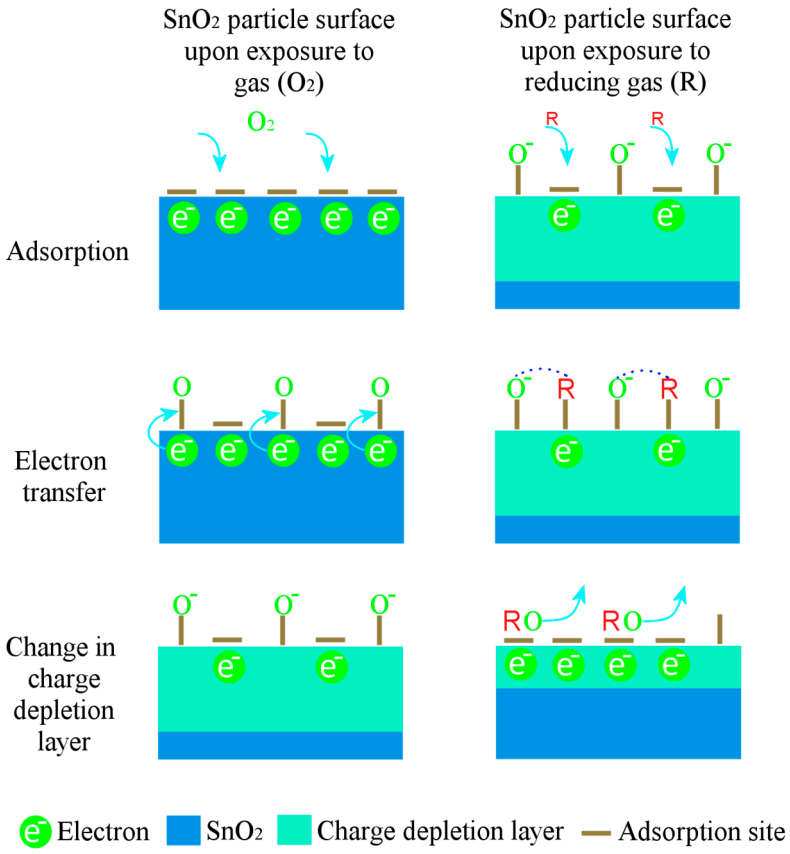

Figure 14. Schematic indicating the sensing mechanism on the SnO_2 surface. Left column indicates reaction with oxygen, whereas right column shows the interaction with reducing gas like CO.

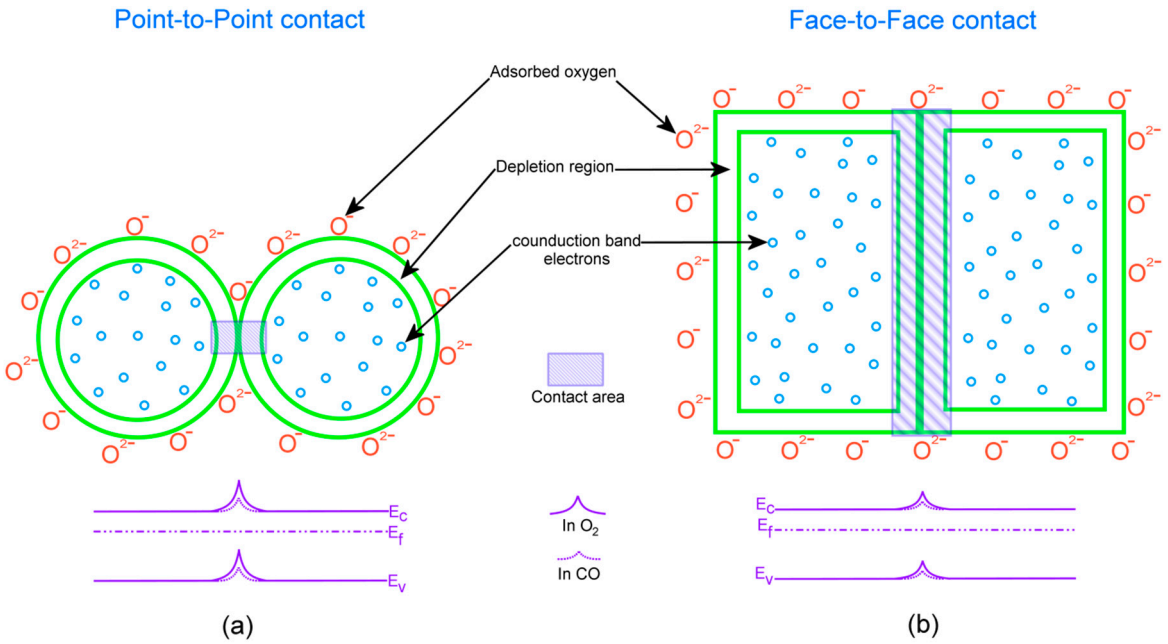

Figure 15: Illustration of the contact area for (a) spherical grains; and (b) tetragonal grains.

Compared to the state of art of the SnO_2 based sensors [20,25,29,31,51,58,60], the CO sensitivity obtained in this work is much higher, a summary of the sensitivities is presented in Table 6. The maximum sensitivity obtained for CO was around 100 and H_2S was around 357. The minimum

operation reported in Table 6 was around 100°C. In our work, we have obtained an increased CO sensitivity (1782) in one order of magnitude for Cu: SnO_2 powders for very low concentrations of CO.

For chemically doped powders, incorporation of additives in the SnO_2 lattice increased the charge carrier concentration which subsequently increased bulk conductivity and decreased the thickness of the space charge region. This effect is clearly observed from our SEM results (Figure 4). During the thermal treatment, presence of dopants gives rise to two important factors, coalescence of the SnO_2 and modification of crystal structure [17,50].Due to *coalescence*, we can observe the increase of the contact area between crystallites and the forming of necks between grains. This will lead to formation of a sensor matrix network [16,69], which is obtained for chemically doped powders. *Modification of crystallographic structure* leads to an increase in crystal defect concentration and a change in crystallographic faceting, these changes will enhance the conductivity of SnO_2 matrix [70,71]. It is evident from the HRTEM results (Figures 7-9) that, stacking faults for Cu and Pt: SnO_2 powders and {221} facets for Pd: SnO_2 powders are observed. It has recently shown by Han et.el [56], that {221} facets show higher sensitivities compared to others. Therefore, the necks formation and the structural modifications produced by to chemical doping have enhanced the sensitivity of the doped SnO_2 pellets. Crystallite size obtained for powders with urea as precipitation agent were relatively uniform and homogenously distributed which increased the surface to volume ratio and further the sensitivity [72].

Table 6. Representative synthesis methods, material characteristics, and corresponding sensitivities for SnO_2 based sensors compared to present work.

SnO_2 synthesis method	**SnO_2 precursor**	**Crystallite size (nm)**	**Sensitivity (Ra/ Rg at specified operating temperature and mole fraction of target gas)**	**Reference**
Vapor–liquid–solid	Sn Powder	~75-90	~ 80 at 300 ˚C and at 10 ppm of CO	[61]
Hydrothermal process	$SnCl_2{\cdot}2H_2O$	~10	~ 78 at 220 ˚C and at 100 ppm of acetone	[62]
Hydrolysis and Precipitation	$SnCl_4.5H_2O$	~15	~80 at 350 ˚C and at 600 ppm of CO	[63]
Chemical spray pyrolysis	$SnCl_4.5H_2O$	~10	~132 at 225 ˚C and at 400 ppm of NO_2	[64]
Precipitation	$SnCl_4.5H_2O$	~14	~100 at 350 ˚C and at 600 ppm of CO	[65]
One-step Solvothermal route	$SnCl_4.5H_2O$	~10	~22.69 at 260 ˚C and at 50 ppm of ethanol gas	[66]
Sol-Gel	$SnCl_4.5H_2O$	~8-20	~1.95 at 100 ˚C and at 5 ppm of CO	[67]
Hydrothermal synthesis	$SnCl_4.5H_2O$	~ 3.4 ± 0.8 nm	~357 at 100 ˚C and at 5 ppm of H_2S	[68]
Present work	$SnCl_4.5H_2O$	~35	~1782 at 300˚C and at 300ppm	--

The sensitivity of the impregnated powders is due to the formation of clusters on the surface of the SnO_2 crystals (Figures 7d and 7f). Therefore, two types of sensitization mechanisms, chemical and electronic, are considered for assuring the effect of clusters on the sensitivity. The detailed explanation of the both mechanisms have been discussed by many authors in detailed previously [73–75], Figure 16 shows both the mechanism in detail. In the electronic mechanism, there is only electronic interaction between the semiconductor and cluster and these interactions change depending on the form of cluster. It has been evidenced that the metal clusters like Cu, Pt and Pd in oxide from can only interact electronically with the SnO_2 and these interactions vanishes if the clusters

are metallic [60]. Since no oxides were observed from our HRTEM results, electronic mechanism can be ruled out. To the best of our knowledge, until now the previous reports[46,75] suggests that the spill over effect (chemical mechanism) lowers the measuring temperature, which could be the possible reason for the increased sensitivity for our impregnated powders at 200 °C (Figures 11 and 12).

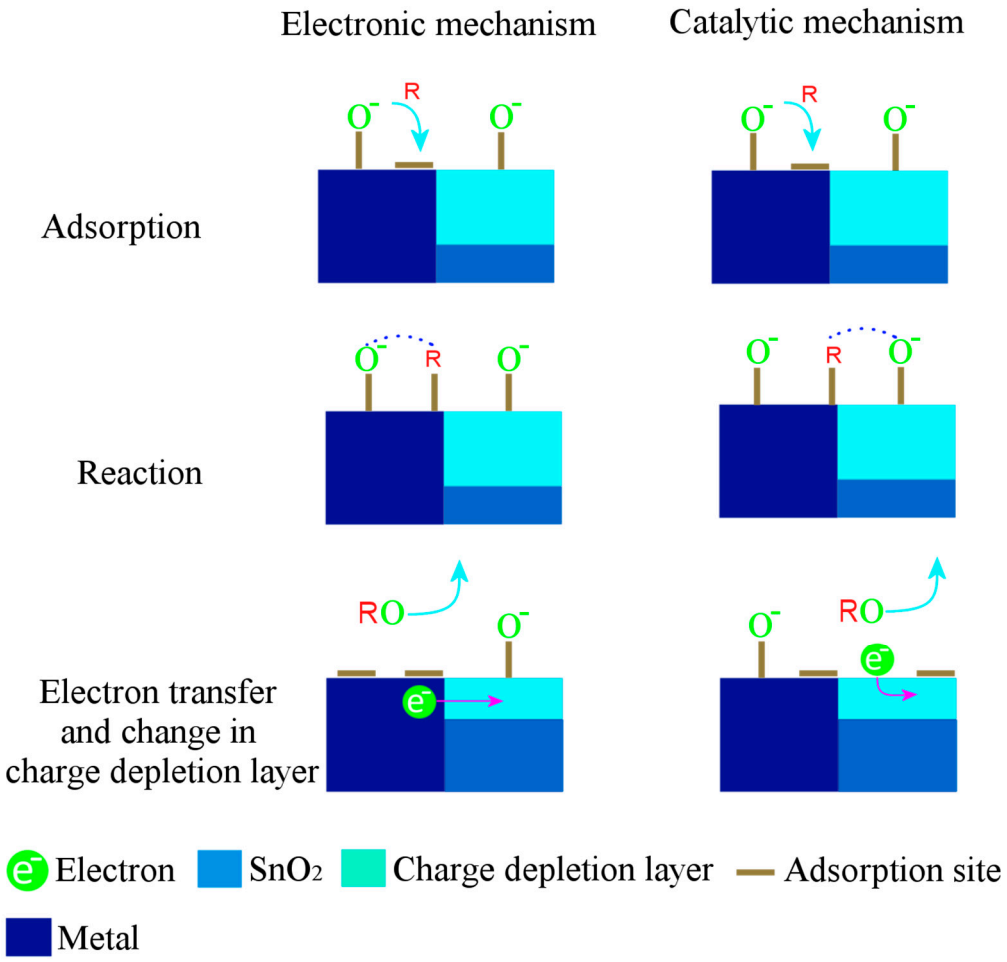

Figure 16. Schematic diagram indicating the general steps involved in the electronic (left column) and catalytic (right column) mechanisms active in SnO_2 sensors with metal additives. *R* represents a reducing gas.

Another important factor that influences the sensitivity is the doping concentration of the additives. In this work, we have utilized 1wt% of concentration for all samples. It has been established that the response of SnO_2 based sensors lies in the range of 0.1-0.6%[41] for the noble metals and for the transition metals it is in the range of 1-4%[48]. However, as we observed form the results obtained in this work, we can conclude that the sensitivity depends on many factors like measuring temperature, microstructure, crystallite size and shape, dopants and on the interaction between the sensing matrix and gas molecules. Further work is necessary to find the exact role of the transition and noble metals as a dopant on the CO sensitivity. A comparison of doping methods and precipitation agents utilized in this work, with their corresponding advantages and sensitivities for the Cu: SnO_2 pellets were represented graphically in Figure 17.

From Figure 13 and Table 5, irrespective of the doping methods and synthesis routes, dopant, Cu showed higher sensitivities than Pt and Pd, which is an interesting and novel result. Therefore, Cu, being a transition metal, its doping has produced better magnitudes of sensitivities in this work than noble metal dopants like Pt and Pd, which were the most effective dopants until now. From this result, it can be concluded that, the fabrication of Cu: SnO_2 sensors will be cost effective way design, while featuring a higher magnitude of CO sensitivity.

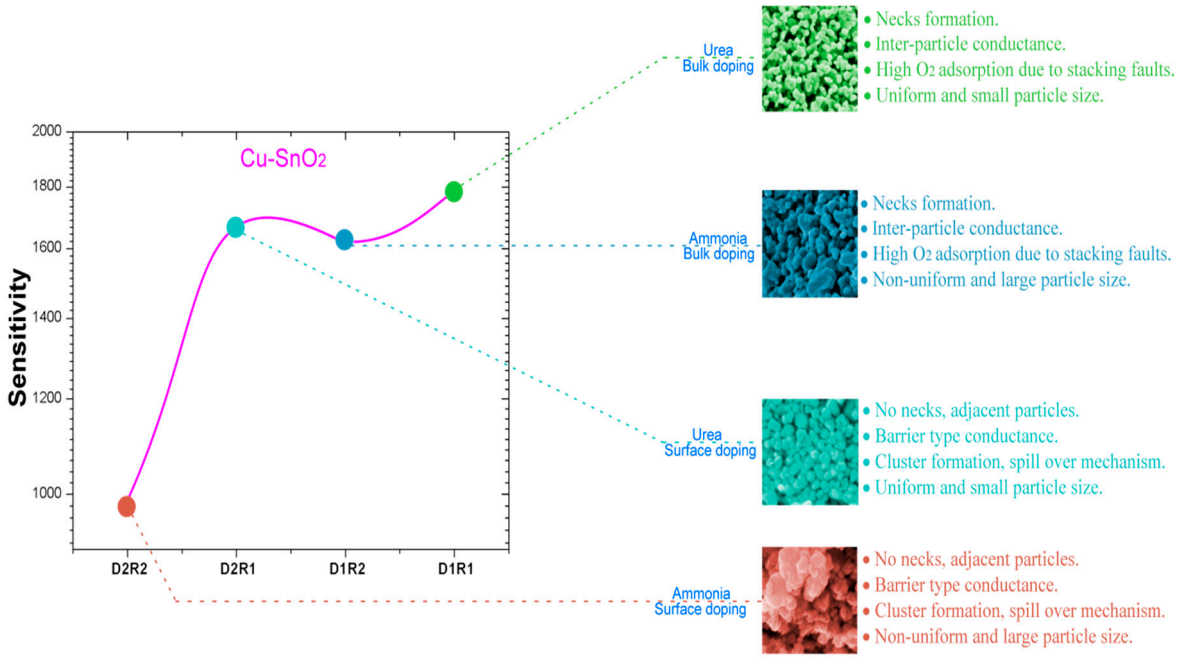

Figure 17. Graphical comparison of synthesis methods of Cu: SnO_2 pellets with corresponding intellects for achieving the high sensitivities.

5. Conclusions

In this work, Cu, Pt and Pd doped SnO_2 powders were successfully synthesized utilizing chemical doping and impregnation methods. Cu, Pt and Pd doped SnO_2 powders crystallite size and porosity was increased respectively compared to the undoped powders, due to the increase in the ionic radii of the dopants. A shift in the (110) SnO_2 plane confirms the incorporation of dopants in the SnO_2 crystal lattice. The intensity of the Raman peaks decreased in the order of undoped, Cu, Pt and Pd: SnO_2. This decrease corresponds to the amount of extraction and compression of Sn-O bonds inside the lattice. Particles size obtained through SEM were around 25-35nm for all the Cu, Pt and Pd doped powders. HRTEM analysis dopant positions and confirms the stacking faults and cluster formation for the powders obtained by chemical doping and impregnation, respectively. Sensitivities of Cu: SnO_2powders are much higher compared to Pt and Pd: SnO_2 powders. Drastic decrease in crystal quality and large number of defects for Pt and Pd: SnO_2 powders reduced their sensitivities in comparison with Cu: SnO_2 powders. Irrespective of doping method, pellets manufactured from the powders synthesized utilizing urea showed high sensitivity than those synthesized ammonia. Additionally, chemically doped sample sensitivities are higher than impregnated ones. The face-to-face contacting form of tetragonal particles enhances the surface-depletion control rather than grain boundary barrier control, which results in a high sensitivity in Cu: SnO_2 powders. The maximum sensitivities obtained is for Cu doped pellets which is around 1782 for powders incorporated by chemical method with Urea as precipitation agent.

Supplementary Materials: The following are available online at www.mdpi.com/link, Figure S1: Schematic diagram of homemade gas sensing system.

Acknowledgments: This work was supported and funded by "Universidad Autonoma del Estado de Hidalgo".

Author Contributions: Conceived and designed the experiments: Venkata Krishna Karthik Tangirala, M. Olvera. Performed the experiments: Venkata Krishna Karthik Tangirala. Analyzed the data: Venkata Krishna Karthik Tangirala, M. Olvera, Ventura rodríguez Lugo, Heberto Gómez Pozos. Wrote the paper: Venkata Krishna Karthik Tangirala, M. Olvera, Heberto Gómez Pozos and Ventura rodríguez Lugo.

Conflicts of Interest: The authors declare no conflict of interest.

References

1. Orozco, L. Gas Detector: Analog Dialogue: Analog Devices **2015**. http://www.analog.com/en/analog-dialogue/articles/designing-low-power-toxic-gas-detector.html.
2. Vetter, S.; Haffer, S.; Wagner, T.; Tiemann, M. Nanostructured Co_3O_4 as a CO gas sensor: Temperature-dependent behavior. *Sensors Actuators B: Chem.* **2015**, *206*, 133–138.
3. Ciureanu, P.; Middelhoek, S.; *Thin Film Resistive Sensors*, 1st ed.; Institute of Physics: Philadelphia, Pa, **1992**; pp.232-345.
4. Marc, J. M.; Morrison, S. R.; Chemical Sensing with Solid State Devices, 1st ed.; Harcourt Brace Jovanovich: London, **2012**; pp. 479-516.
5. Yamazoe, N.; Fuchigami, J.; Kishikawa, M.; Seiyama, T. Interactions of tin oxide surface with O_2, H_2O and H_2. *Surf. Sci.* **1979**, *86*, 335–344.
6. Heiland, G. Homogeneous semiconducting gas sensors. *Sensors Actuators* **1981**, *2*, 343–361.
7. Morrison, S. R. Semiconductor gas sensors. *Sensors Actuators* **1981**, *2*, 329–341.
8. Patent US3631436 - Gas-detecting device - Google Patents **2015**.
9. Wagner, C. Physical Chemistry of Ionic Crystals Involving Small Concentrations of Foreign Substances. *J. Phys. Chem.* **1953**, *57*, 738–742.
10. Barth, S.; Hernandez-Ramirez, F.; Holmes, J. D.; Romano-Rodriguez, A. Synthesis and applications of one-dimensional semiconductors. *Prog. Mater. Sci.* **2010**, *55*, 563–627.
11. Choi, K.J.; Jang, H.W. One-Dimensional Oxide Nanostructures as Gas-Sensing Materials: Review and Issues. *Sensors* **2010**, *10*, 4083-4099.
12. Huang, X.-J.; Choi, Y.-K. Chemical sensors based on nanostructured materials. *Sensors Actuators B: Chem.* **2007**, *122*, 659–671.
13. Mathur, S.; Ganesan, R.; Grobelsek, I.; Shen, H.; Ruegamer, T.; Barth, S. Plasma-Assisted Modulation of Morphology and Composition in Tin Oxide Nanostructures for Sensing Applications. *Adv. Eng. Mater.* **2007**, *9*, 658–663.
14. Gas'kov, A. M.; Rumyantseva, M. N. Nature of Gas Sensitivity in Nanocrystalline Metal Oxides **2001**, *74*.
15. Zhang, S.; Sun, D.; Fu, Y.; Du, H. Recent advances of superhard nanocomposite coatings: a review. *Surf. Coatings Technol.* **2003**, *167*, 113–119.
16. Korotcenkov, G. Practical aspects in design of one-electrode semiconductor gas sensors: Status report. *Sensors Actuators B: Chem.* **2007**, *121*, 664–678.
17. Korotcenkov, G. Gas response control through structural and chemical modification of metal oxide films: state of the art and approaches. *Sensors Actuators B: Chem.* **2005**, *107*, 209–232.
18. Korotcenkov, G.; Cho, B. K. Thin film SnO2-based gas sensors: Film thickness influence. *Sensors Actuators B: Chem.* **2009,** *142*, 321–330.
19. Yang, D; Nanocomposite Films for Gas Sensing. *InTechOpen.* **2015**, 1, 857-882.
20. Camargo, P. H. C.; Satyanarayana, K. G.; Wypych, F. Nanocomposites: synthesis, structure, properties and new application opportunities. *Mater. Res.* **2009**, *12*, 1–39.
21. Fang, H.; Miller, T. M.; Magruder, R. H.; Weller, R. A. The effect of strain on the resistivity of indium tin oxide films prepared by pulsed laser deposition. *J. Appl. Phys.* **2002**, *91*, 6194–6196.
22. Vaishnav, V. S.; Patel, P. D.; Patel, N. G. Indium Tin Oxide thin film gas sensors for detection of ethanol vapours. *Thin Solid Films* **2005**, *490*, 94–100.
23. Gorley, P. M.; Khomyak, V. V.; Bilichuk, S. V.; Orletsky, I. G.; Horley, P. P.; Grechko, V. O. SnO2 films: formation, electrical and optical properties. *Mater. Sci. Eng. B* **2005**, *118*, 160–163.

24. Yoo, K. S.; Park, S. H.; Kang, J. H. Nano-grained thin-film indium tin oxide gas sensors for H2 detection. *Sensors Actuators B: Chem.* **2005**, *108*, 159–164.
25. Vasu, V.; Subrahmanyan, A. Physical properties of sprayed SnO2 films. *Thin Solid Films* **1991**, *202*, 283–288.
26. Zhang, G.; Liu, M. Effect of particle size and dopant on properties of SnO2-based gas sensors. *Sensors Actuators B: Chem.* **2000**, *69*, 144–152.
27. Korotcenkov, G.; Brinzari, V.; Boris, I. (Cu, Fe, Co, or Ni)-doped tin dioxide films deposited by spray pyrolysis: doping influence on film morphology. *J. Materials Sci.* **2008**, *43*, 2761–2770.
28. Mädler, L.; Sahm, T.; Gurlo, A.; Grunwaldt, J.-D.; Barsan, N.; Weimar, U.; Pratsinis, S. E. Sensing low concentrations of CO using flame-spray-made Pt/SnO2 nanoparticles. *J. Materials Sci.* **2006**, *8*, 783–796.
29. Fang, G.; Liu, Z.; Zhang, Z.; Hu, Y.; Ashur, I. A.; Yao, K. L. Preparation of SnO_2-CuO nanocrystalline powders in two different ways by the sol-gel method. *Phys. Status solidi* **1996**, *156*, 15–22.
30. Cirera, A.; Vilà, A.; Diéguez, A.; Cabot, A.; Cornet, A.; Morante, J. R. Microwave processing for the low cost, mass production of undoped and in situ catalytic doped nanosized SnO_2 gas sensor powders. *Sensors Actuators B: Chem.* **2000**, *64*, 65–69.
31. Song, K. C.; Kang, Y. Preparation of high surface area tin oxide powders by a homogeneous precipitation method. *Mater. Lett.* **2000**, *42*, 283–289.
32. Déchamps, M.; Djuriçić, B.; Pickering, S. Structure of Zirconia Prepared by Homogeneous Precipitation. *J. Am. Ceram. Soc.* **1995**, *78*, 2873–2880.
33. Karthik, T. V. K. ; Maldonado, A. ; de la L. Olvera, M. ; Synthesis of tin oxide powders by homogeneous precipitation. Structural and morphological characterization. In *Electrical Engineering, Computing Science and Automatic Control (CCE), 2013 10th International Conference on*; **2012**; pp. 1–8.
34. Karthik, T. V. K.; Maldonado, A.; de la L Olvera, M. Manufacturing of tin oxide pellets and their application for CO and C_3H_8 gas sensors. In *Electrical Engineering, Computing Science and Automatic Control (CCE), 2013 10th International Conference on*; **2013**; pp. 402–406.
35. Haines, J.; Léger, J. M.; X-ray diffraction study of the phase transitions and structural evolution of tin dioxide at high pressure: Relationships between structure types and implications for other rutile-type dioxides. *Phys. Rev. B*. **1997**, *55*, 11144.
36. Giri, P. K.; Bhattacharyya, S.; Singh, D. K.; Kesavamoorthy, R.; Panigrahi, B. K.; Nair, K. G. M. Correlation between microstructure and optical properties of ZnO nanoparticles synthesized by ball milling. *J. Appl. Phys.* **2007,** *102*.
37. Patterson, A. L.; The Diffraction of X-Rays by Small Crystalline Particles. *Phys. Rev.* **1939**, *56*, 972.
38. Cullity, B.D; Stock, S.R. *Elements of X-Ray Diffraction*, 3rd ed; Pearson: USA, **2001**; Volume 3, pp. 294–366.
39. Dar, M. A.; Batoo, K. M.; Verma, V.; Siddiqui, W. A.; Kotnala, R. K. Synthesis and characterization of nano-sized pure and Al-doped lithium ferrite having high value of dielectric constant. *J. Alloy. Compd.* **2010**, *493*, 553–560.
40. Shannon, R. D. Revised effective ionic radii and systematic studies of interatomic distances in halides and chalcogenides. *Acta Crystallogr. Sect. A: Cryst. Physics, Diffraction, Theor. Gen. Crystallogr.* **1976**, *32*, 751–767.
41. Jarzebski, Z. M.; Marton, J. P. Physical Properties of SnO2 Materials: I. Preparation and Defect Structure. *J. Electrochem. Soc.* **1976**, *123*, 199–205.
42. Traylor, J. G.; Smith, H. G.; Nicklow, R. M.; and Wilkinson, M. K.; Lattice Dynamics of Rutile 2015. *Phys. Rev. B* **1971**, 3, 3457.
43. Srinivas, K.; Vithal, M.; Sreedhar, B.; Raja, M. M.; Reddy, P. V. Structural, Optical, and Magnetic Properties of Nanocrystalline Co Doped SnO_2 Based Diluted Magnetic Semiconductors. *J. Phys. Chem. C* **2009**, *113*, 3543–3552.

44. Katiyar, R. S. Dynamics of the rutile structure. I. Space group representations and the normal mode analysis. *J. Phys. C: Solid State Phys.* **1970**, *3*, 1087-1096.
45. Wang, W.; Xu, C.; Wang, G.; Liu, Y.; Zheng, C. Synthesis and Raman scattering study of rutile SnO2 nanowires. *J. Appl. Phys.* **2002**, *92*, 2740–2742.
46. Azam, A.; Ahmed, A. S.; Habib, S. S.; Naqvi, A. H. Effect of Mn doping on the structural and optical properties of SnO2 nanoparticles. *J. Alloy. Compd.* **2012**, *523*, 83–87.
47. Fliegel, W.; Behr, G.; Werner, J.; Krabbes, G. Preparation, development of microstructure, electrical and gas-sensitive properties of pure and doped SnO_2 powders **1994**, *19*, 474–477.
48. Matsuura, Y.; Takahata, K. Stabilization of SnO_2 sintered gas sensors. *Sensors Actuators B: Chem.* **1991**, *5*, 205–209.
49. Lifshitz, I. M.; Slyozov, V. V. The kinetics of precipitation from supersaturated solid solutions. *J. Phys. Chem. Solids* **1961**, *19*, 35–50.
50. Korotcenkov, G.; Cornet, A.; Rossinyol, E.; Arbiol, J.; Brinzari, V.; Blinov, Y. Faceting characterization of tin dioxide nanocrystals deposited by spray pyrolysis from stannic chloride water solution. *Thin Solid Films* **2005**, *471*, 310–319.
51. Liu, Y.; Dong, J.; Liu, M. Well-Aligned "Nano-Box-Beams" of SnO2. *Adv. Mater.* **2004**, *16*, 353–356.
52. Zhong, Z.; Yin, Y.; Gates, B.; Xia, Y. Preparation of Mesoscale Hollow Spheres of TiO_2 and SnO_2 by Templating Against Crystalline Arrays of Polystyrene Beads. *Adv. Mater.* **2000**, *12*, 206–209.
53. McAleer, J. F.; Moseley, P. T.; Norris, J. O. W.; Williams, D. E. Tin dioxide gas sensors. Part 1. —Aspects of the surface chemistry revealed by electrical conductance variations. *J. Chem. Soc., Faraday Trans. 1* **1987**, *83*, 1323–1346.
54. Martinez, C. J.; Hockey, B.; Montgomery, C. B.; Semancik, S. Porous tin oxide nanostructured microspheres for sensor applications. *Langmuir: ACS J. surfaces colloids* **2005**, *21*, 7937–7944.
55. Batzill, M.; Katsiev, K.; Diebold, U. Surface morphologies of SnO_2. *Surf. Sci.* **2003**, *529*, 295–311.
56. Han, X.; Jin, M.; Xie, S.; Kuang, Q.; Jiang, Z.; Jiang, Y.; Xie, Z.; Zheng, L. Synthesis of Tin Dioxide Octahedral Nanoparticles with Exposed High-Energy {221} Facets and Enhanced Gas-Sensing Properties. *Angew. Chem.* **2009**, *121*, 9344–9347.
57. Alim, K. A.; Fonoberov, V. A.; Shamsa, M.; Balandin, A. A. Micro-Raman investigation of optical phonons in ZnO nanocrystals. *J. Appl. Phys.* **2005**, *97*, 124313, 1-5.
58. Zheng, J. G. Dislocations in nanocrystalline SnO2 thin films. *Philos. Mag. Lett.* **1996**, *73*, 93–100.
59. Lee, J. H. Gas sensors using hierarchical and hollow oxide nanostructures: Overview. *Sensors Actuators, B: Chem.* **2009**, *140*, 319–336.
60. Lee, J.-H. Gas sensors using hierarchical and hollow oxide nanostructures: Overview. *Sensors Actuators B: Chem.* **2009**, *140*, 319–336.
61. Choi, S.-W.; Katoch, A.; Sun, G.-J.; Kim, J.-H.; Kim, S.-H.; Kim, S. S. Dual Functional Sensing Mechanism in SnO2–ZnO Core–Shell Nanowires. *ACS Appl. Mater. & Interfaces* **2014**, *6*, 8281–8287.
62. Wang, X.; Wang, Y.; Tian, F.; Liang, H.; Wang, K.; Zhao, X.; Lu, Z.; Jiang, K.; Yang, L.; Lou, X. From the Surface Reaction Control to Gas-Diffusion Control: The Synthesis of Hierarchical Porous SnO2 Microspheres and Their Gas-Sensing Mechanism. *J. Phys. Chem. C* **2015**, *119*, 15963–15976.
63. Ma, N.; Suematsu, K.; Yuasa, M.; Shimanoe, K. Pd Size Effect on the Gas Sensing Properties of Pd-Loaded SnO2 in Humid Atmosphere. *ACS Appl. Mater. & Interfaces* **2015**, *7*, 15618–15625.
64. Kumar, M.; Kumar, A.; Abhyankar, A. C. Influence of Texture Coefficient on Surface Morphology and Sensing Properties of W-Doped Nanocrystalline Tin Oxide Thin Films. *ACS Appl. Mater. & Interfaces* **2015**, *7*,

3571–3580.

65. Ma, N.; Suematsu, K.; Yuasa, M.; Kida, T.; Shimanoe, K. Effect of Water Vapor on Pd-Loaded SnO_2 Nanoparticles Gas Sensor. *ACS Appl. Mater. & Interfaces* **2015**, *7*, 5863–5869.
66. Sun, Z. P.; L Liu, L. Z., DZ Jia Rapid synthesis of ZnO nano-rods by one-step, room-temperature, solid-state reaction and their gas-sensing properties. *Nanotechnology* **2006**, *17*, 2266-2270.
67. Lian, Y.; Liu, S.; Hu, Q. Sensors for carbon monoxide based on Pd/SnO2/CNT nanocomposites. *Phys. Status solidi* **2014**, *211*, 2729–2734.
68. Chen, Y.; Ma, J.; Mei, L. Gas Sensing of SnO_2 Nanocrystals Revisited: Developing Ultra-Sensitive Sensors for Detecting the H_2S Leakage of Biogas. *Sci. Reports* **2014**, *4*,1-8.
69. Korotcenkov, G. Metal oxides for solid-state gas sensors: What determines our choice? *Mater. Sci. Eng. B* **2007**, *139*, 1–23.
70. Wang, N.; Cai, Y.; Zhang, R. Q. Growth of nanowires. *Mater. Sci. Eng. R: Reports* **2008**, *60*, 1–51.
71. Gryaznov, V. G.; Trusov, L. I. Size effects in micromechanics of nanocrystals. *Prog. Mater. Sci.* **1993**, *37*, 289–401.
72. Mulla, I. S.; Ramgir, N. S.; Hwang, Y. K.; Chang, J.-S. Semiconductor Tin Oxide Gas Sensors: From Bulk to Thin Films. *J. Ind. Eng. Chem.* **2004**, *10*, 1242–1256.
73. Brinzari, V.; Korotcenkov, G.; Schwank J.; Boris, Y.; Chemisorptional approach to kinetic analysis of SnO_2: Pd-based thin film gas sensors. *Journal of Optoelectronics and Advanced Materials*. **2002**, 4, 147 - 150.
74. Kolmakov, A.; Chen, X.; Moskovits, M.; Functionalizing Nanowires with Catalytic Nanoparticles for Gas Sensing Application. *J Nanosci Nanotechnol.* **2008**, 8, 111-21.
75. Matsushima, S.; Maekawa, T.; Tamaki, J.; Miura, N.; Yamazoe, N. New methods for supporting palladium on a tin oxide gas sensor. *Sensors Actuators B: Chem.* **1992**, *9*, 71–78.